

# Microscopic dynamics of lithium diffusion in single crystal of the solid-state electrolyte $\text{La}_{2/3-x}\text{Li}_{3x}\text{TiO}_3$ ( $x = 0.13$ ) studied by quasielastic neutron scattering

Masato Matsuura\*,<sup>1</sup> Yasuyuki Fujiwara,<sup>2</sup> Hiroki Moriwake,<sup>3</sup> Koji Ohara,<sup>4</sup> and Yukinobu Kawakita<sup>5</sup>

<sup>1</sup>*Neutron Science and Technology Center, Comprehensive Research Organization for Science and Society (CROSS), Tokai, Ibaraki 319-1106, Japan\**

<sup>2</sup>*Faculty of Engineering, Shinshu University, Nagano 380-8553, Japan*

<sup>3</sup>*Nanostructures Research Laboratory, Japan Fine Ceramics Center, Nagoya 456-8587, Japan*

<sup>4</sup>*Research and Utilization Division, Japan Synchrotron Radiation Research Institute (SPring-8/JASRI), Sayo, Hyogo 679-5198, Japan*

<sup>5</sup>*Materials and Life Science Division, J-PARC Center, JAEA, Tokai, Ibaraki 319-1195, Japan*

(Dated: November 25, 2021)

Quasi-elastic neutron scattering (QENS) measurements combined with first principles based molecular-dynamics calculations were conducted to study the dynamics of  $\text{Li}^+$  ions in a solid-state electrolyte  $\text{La}_{2/3-x}\text{Li}_{3x}\text{TiO}_3$  (LLTO) with  $x = 0.13$ . By using a large  $^7\text{Li}$ -enriched single crystal sample, a QENS signal was clearly observed along the three principal axes [110], [111], and [001] at a temperature ( $T$ ) of 600 K. Wave vector dependence of the line width of the QENS signal along each direction was explained well using the Chudley-Elliott model for jumps between the  $A$  sites of the perovskite lattice through the bottleneck square, which was also supported by molecular dynamics calculations. At  $T = 600$  K, the estimated self-diffusion coefficient of  $\text{Li}^+$  ( $D_{\text{Li}}$ ) in the  $ab$ -plane [ $D_{\text{Li}}^{ab} = (6.8 \pm 0.5) \times 10^{-6} \text{ cm}^2/\text{s}$ ] was slightly larger than that along the  $c$  axis [ $D_{\text{Li}}^c = (4.4 \pm 0.3) \times 10^{-6} \text{ cm}^2/\text{s}$ ], suggesting quasi-isotropic diffusion, that is, the three-dimensional diffusion of  $\text{Li}^+$  ions. The decrease in  $D_{\text{Li}}$  with decreasing  $T$  was reasonably explained by a thermal activation process with the activation energy determined from ionic-conductivity measurements. Furthermore, the estimated values of the self-diffusion coefficient of  $\text{Li}^+$  ions are comparable to those in the sulfide-based  $\text{Li}^+$  ion conductor,  $\text{Li}_7\text{P}_3\text{S}_{11}$ , although its ionic conductivity is 10 times larger than that for LLTO. The obtained microscopic information on  $\text{Li}^+$  diffusion in LLTO clarifies how to understand the Li conduction mechanism in LLTO and  $\text{Li}_7\text{P}_3\text{S}_{11}$  in a unified manner and can provide a way to increase the  $\text{Li}^+$  ionic conductivity in oxide-based solid electrolytes.

## I. INTRODUCTION

An all-solid-state lithium-ion battery has been heavily investigated as a next-generation energy storage system [1, 2], because both the energy density and safety of such all-solid-state batteries are expected to be drastically improved by replacing an organic solvent-based liquid electrolyte with a solid electrolyte. Sulfide-based  $\text{Li}^+$  ionic conductors, such as  $\text{Li}_{10}\text{GeP}_2\text{S}_{12}$  (LGPS), are considered to be promising candidates for a solid electrolyte because of their extremely high  $\text{Li}^+$  ionic conductivity ( $\sigma_{\text{Li}}$ ) ranging approximately  $10^{-2} \text{ S/cm}$  at room temperature, which is comparable to the  $\sigma_{\text{Li}}$  of typical liquid electrolytes [3]. By contrast,  $\sigma_{\text{Li}}$  of oxide-based  $\text{Li}^+$  ionic conductors is more than one order of magnitude lower than that of sulfide-based  $\text{Li}^+$  ionic conductors such as LGPS,  $\text{Li}_3\text{PS}_4$ , and  $\text{Li}_7\text{P}_3\text{S}_{11}$  as summarized in Table I. Because oxide-based  $\text{Li}^+$  ionic conductors have an excellent stability in air, it is highly desirable to develop oxide-based  $\text{Li}^+$  ionic conductors with a high  $\sigma_{\text{Li}}$ .

Among the many oxide-based  $\text{Li}^+$  ionic conductors,  $\text{La}_{2/3-x}\text{Li}_{3x}\text{TiO}_3$  (LLTO) exhibits the highest  $\sigma_{\text{Li}}$  at room temperature [4–6]. Since LLTO poses a simple double-perovskite structure [see Fig. 1(a)], LLTO is considered an ideal system for studying the relationship

between the  $\text{Li}^+$  conduction mechanism and structural properties in solids. Previous extensive structural studies on LLTO revealed the following key features on  $\sigma_{\text{Li}}$  [5, 7–13]. First,  $\sigma_{\text{Li}}$  is closely related to the La and defect contents at the  $A$  site in a double-perovskite lattice, in which the La-rich and La-poor layers are stacked alternately along the  $c$  axis.  $\text{Li}^+$  ions mainly conduct through the La-poor layer, when the Li concentration is low (or  $x < 0.08$ ) [5, 9–12]. The difference in the La occupancy between the La-rich and La-poor layers decreases with the Li content. A nearly three-dimensional diffusion is expected for an Li-rich composition. Second,  $\sigma_{\text{Li}}$  strongly depends on the size of the “bottleneck” square surrounded by oxygen ions. The potential barrier of  $\sigma_{\text{Li}}$  is dominated by the repulsion energy from oxygen ions [11, 13].

Unfortunately, these findings are based on the time-averaged structure and do not provide direct information on the dynamics of  $\text{Li}^+$  ions. However, neutron scattering can detect the motion of  $\text{Li}^+$  ions as quasielastic neutron scattering (QENS). When a neutron is scattered by a mobile  $\text{Li}^+$  ion, neutron energy is transferred to, or from, the  $\text{Li}^+$  ions, resulting in broadening of the elastic signal. The wave vector ( $Q$ ) dependence of the line-width of the QENS provides detailed information on the dynamical conduction path of  $\text{Li}^+$  on a microscopic scale, such as the residence time ( $\tau$ ) and jump vector ( $l$ ). Furthermore, if a single crystal is available, directional information of

\* m.matsuura@cross.or.jp

$\text{Li}^+$  jump can be obtained. However, such a detailed QENS study using a single crystal has not been reported thus far perhaps owing to a lack of sufficiently large single crystals and weak QENS signals from mobile  $\text{Li}^+$  ions.

In this paper, we present a QENS study on the dynamics of  $\text{Li}^+$  ions using a single crystal of LLTO and a state-of-the-art neutron backscattering spectrometer. Combined with a molecular dynamics (MD) simulation using first-principles calculations, the dynamical conduction path and direction dependent self-diffusion coefficient of  $\text{Li}^+$  ions ( $D_{\text{Li}}$ ) at a microscopic scale have been directly extracted from QENS data.

## II. EXPERIMENTAL DETAILS

A powder sample of  $^7\text{Li}$ -enriched LLTO was synthesized using a solid-state reaction technique for the stoichiometric mixtures of  $^7\text{Li}$ -enriched  $\text{Li}_2\text{CO}_3$  (99.9%, Cambridge Isotope Laboratories, Inc.),  $\text{La}_2\text{O}_3$  (99.9%, Miike Smelting Co., Ltd.), and  $\text{TiO}_2$  (99.9%, Toho Titanium Co., Ltd.). The quality of the obtained LLTO powder was confirmed by powder x-ray diffraction measurements (SmartLab, Rigaku Corporation), as shown in Fig. S1 in the Supplemental Material [19]. Bulk single crystals of  $^7\text{Li}$ -enriched LLTO were grown using a directional solidification method under a growth condition recently reported for  $\text{Li}_x\text{La}_{(1-x)/3}\text{NbO}_3$  [21]. The sample is stable in the air with no reaction to moisture. The composition  $x$  of the sample was determined as  $x = 0.13$  using an inductivity-coupled plasma optical emission spectrometer. The obtained LLTO crystals were cut perpendicular to the growth direction to create a disk with a 20 mm diameter and 1.5 mm thickness. The orientation of each disk was checked in 5 mm steps using an x-ray Laue diffractometer. Six disks consisting of only a single domain with the same crystal orientation were stacked and fixed using hydrogen-free glue (CYTOP). The total weight and volume of the stacked discs were 6.7 g and  $\sim 1$  cc, respectively. Multiple scattering effect was not considered because the fraction of multiple scattering was as small as 10% estimated by approximating a cylindrical sample shape [22]. Resolution-limited Bragg peaks were confirmed by neutron experiments, which guarantees a bulk single grain of the stacked disk-shape crystals.

All first-principles calculations were conducted within a generalized gradient approximation revised for solids, as developed by Perdew, Burke, and Ernzerhof [23], within the framework of the density functional theory [24, 25], using the plane-wave basis projector augmented wave (PAW) method [26]. For the PAW potentials,  $2s$  and  $2p$  electrons for O,  $3p$ ,  $3d$ , and  $4s$  electrons for Ti, and  $4f$ ,  $5s$ ,  $5p$ ,  $5d$ , and  $6s$  electrons for La were explicitly treated as valence electrons, with a plane-wave cutoff energy of 500 eV. Unit cells of the tetragonal  $(\text{La}_{0.5}\text{Li}_{0.5})\text{TiO}_3$  [ $(\text{La}_1\text{Li}_1)\text{Ti}_2\text{O}_6$ ] ( $P4/mmm$ ) structure were assumed and relaxed using a  $7 \times 7 \times 4$   $k$ -point mesh within the Brillouin zones generated using the

Monkhorst-Pack scheme, and a convergence criterion for residual forces of 0.01 eV/Å. In this study, all first-principles molecular dynamics (FPMD) simulations were performed by Vienna ab initio simulation package (VASP) code [27, 28]. Supercells for FPMD simulations for the Li migration trajectory were constructed from  $2 \times 2 \times 1$  unit cells of the relaxed tetragonal ( $P4/mmm$ ) structure with one Li vacancy for Li migration. The total number of electrons for the FPMD supercell was adjusted to keep the system insulating. FPMD production runs were performed within the canonical ensemble (constant volume, temperature and number of atoms) using a Nosé-Hoover thermostat [29] at temperatures ( $T$ ) of 1000 K, with a time step of 1 fs. The calculated temperature, ion-electron energy, and kinetic energy were stable as a function of the simulation steps, demonstrating the stability of FPMD simulations (Figs. S2-S4 in the Supplemental Material [19]). The structures were relaxed for 2 ps (2000 steps) to ensure that thermodynamic equilibrium had been reached before applying production runs of 40 ps (40,000 steps) for the Li migration trajectory.

QENS measurements were conducted using a time-of-flight near-backscattering spectrometer, **DNA** installed at the J-PARC MLF [30]. The final neutron energy of 2.08 meV was selected using Si (111) analyzers and a Bragg angle of  $87.5^\circ$ . A pulse shaping chopper rotating at 300 Hz with 3 cm slit provided an elastic resolution of  $2.5 \mu\text{eV}$  and an energy transfer ( $E$ ) range of  $-20 < E < 80 \mu\text{eV}$ . Neutron scattering data were obtained using the UTSUSEMI software [31]. The stacked single crystal sample was sealed in an aluminum can with air and mounted to access the ( $hhl$ ) horizontal scattering plane. There are some controversies in the structure of LLTO. For the high Li-doped sample near  $x = 0.13$ , tetragonal cell with  $a(\sim 2^{1/2}a_p) \times a(\sim 2^{1/2}a_p) \times c(\sim 2a_p)$ , [32] where  $a_p$  is a lattice parameter of cubic unit cell, simple tetragonal cell with  $a(\sim a_p) \times a(\sim a_p) \times c(\sim 2a_p)$ , [33] and orthogonal cell with  $a(\sim 2a_p) \times b(\sim 2a_p) \times c(\sim 2a_p)$  [11, 20] have been proposed. Throughout this paper, we label the momentum transfer in units of the reciprocal lattice vectors  $a^* = b^* = 1.147 \text{ \AA}^{-1}$  and  $c^* = 0.811 \text{ \AA}^{-1}$  in the orthogonal notation. Figure 1(b) shows three scan trajectories in the horizontal scattering plane ( $hhl$ ). The sample was rotated to make scattering trajectories nearly parallel to the three principal axes [110], [111], and [001] below  $Q < 1.2 \text{ \AA}^{-1}$ . The scattering intensity along the vertical direction was integrated for  $-0.2 < k < 0.2$  r.l.u. in  $(0, k, -k)$ .

## III. RESULTS

The QENS spectra at  $(-0.8, -0.8, 0)$  at various  $T$ 's are plotted in the logarithmic scale in Fig. 2. Because  $\text{Li}^+$  ions are expected to be immobile at  $T = 150$  K, we assume that the spectrum at  $T = 150$  K corresponds to a delta function convoluted with the instrumental resolution. A similar resolution-limited spectrum is also

TABLE I. Comparison of ionic conductivity ( $\sigma_{\text{Li}}$ ), activation energy ( $E_a$ ), and diffusion coefficient ( $D_{\text{Li}}$ ) for LGPS,  $\text{Li}_3\text{PS}_4$ ,  $\text{Li}_7\text{P}_3\text{S}_{11}$  (glass), and LLTO.  $\sigma_{\text{Li}}$  and  $E_a$  are the values at room temperature (RT).  $D_{\text{Li}}$ 's for LGPS and  $\text{Li}_3\text{PS}_4$  are the reported values obtained from pulsed field gradient nuclear magnetic resonance measurements, whereas  $D_{\text{Li}}$ 's for  $\text{Li}_7\text{P}_3\text{S}_{11}$  and LLTO are obtained from QENS measurements. \* $D_{\text{Li}}$  at  $T = 473$  K for  $\text{Li}_3\text{PS}_4$  and LLTO are estimated using the Arrhenius law with  $E_a$ .

Systems	$\sigma_{\text{Li}}$ (S/cm)	$E_a$ (eV)	$D_{\text{Li}}$ ( $\text{cm}^2/\text{sec}$ )
LGPS	$1.2 \times 10^{-2}$ [3]	0.25 [3]	$3 \times 10^{-8}$ (RT) [14] $6 \times 10^{-7}$ ( $T = 473$ K)
$\text{Li}_3\text{PS}_4$	$2 \times 10^{-4}$ [15]	0.35 [15]	$9 \times 10^{-10}$ (RT), [16] * $2.9 \times 10^{-8}$ ( $T = 473$ K)
$\text{Li}_7\text{P}_3\text{S}_{11}$ (glass)	$0.91 \times 10^{-3}$ [17]	0.44 [17]	$5.7 \times 10^{-6}$ ( $T = 473$ K) [18]
LLTO	$7 \times 10^{-5}$ [5]	0.4 ( $T < 400$ K), 0.15 ( $T > 400$ K) [5]	$6.8 \times 10^{-6}$ ( $T = 600$ K), * $3.1 \times 10^{-6}$ ( $T = 473$ K)

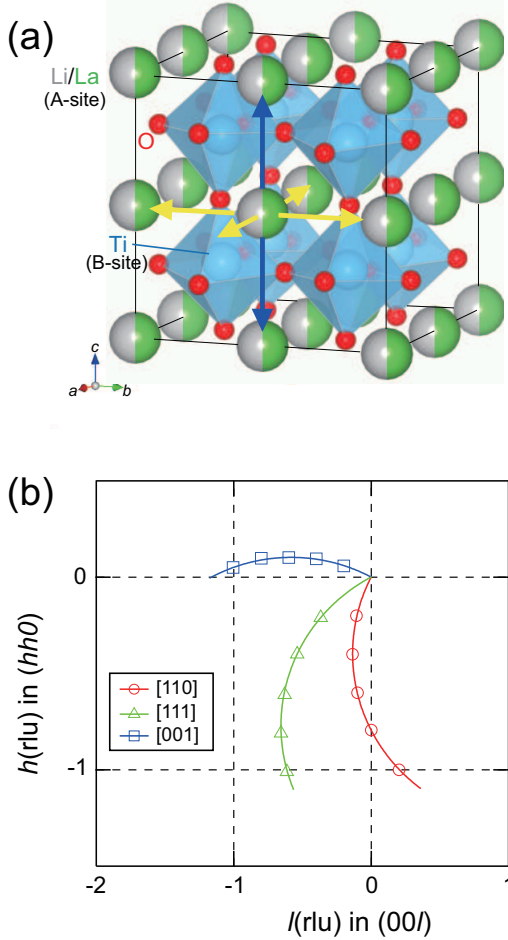


FIG. 1. (color online) (a) Crystal structure of LLTO. Arrows in (a) indicate jump vectors of  $\text{Li}^+$  ions. (b) Scan trajectory of neutron measurements.

obtained at  $T = 300$  K, suggesting that the  $\text{Li}^+$  ions are still immobile even at  $T = 300$  K within the energy or time resolution of the current setup ( $2.5 \mu\text{eV} \sim 0.6 \text{ GHz} \sim 0.5 \text{ ns}$ ). At  $T \geq 410$  K, the intensity of the elastic peak decreases with increasing  $T$  (see the inset of Fig. 2), whereas the scattering intensities for  $|E| > 4 \mu\text{eV}$

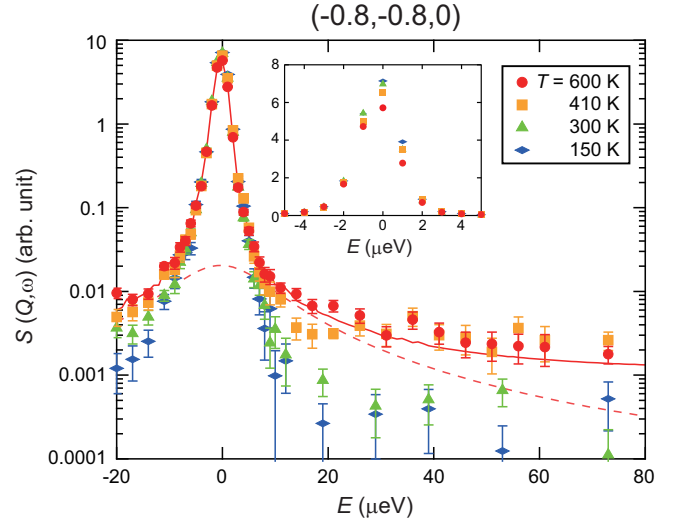


FIG. 2. (color online) QENS spectra at  $(-0.8, -0.8, 0)$  for  $^7\text{LLTO}$  measured at  $T = 150, 300, 410,$  and  $600$  K. The inset shows enlarged data near  $E = 0$  in a linear scale. Scattering intensities for  $-0.9 < h < -0.7$  r.l.u. in  $(hh0)$  are averaged. The solid line indicates a fit with the sum of Lorentzian and delta functions, and a flat background. The  $T = 150$  K data were convoluted to the delta and Lorentzian functions as an instrumental resolution. The dotted line represents the Lorentzian function for the fitting to the 600 K data.

are enhanced with  $T$ . This suggests the dynamic nature of  $\text{Li}^+$  ions at  $T \geq 410$  K. These spectra were fitted with the sum of a Lorentzian and a delta function convoluted with the resolution function estimated from the  $T = 150$  K data in addition to a flat background. Although the QENS component, i.e., the Lorentzian component, is 1000 times weaker than the elastic peak, the QENS component, represented by a dotted line in Fig. 2, is clearly extracted, mainly owing to the low background of the DNA spectrometer. Note that the half width at half maximum ( $\Gamma$ ) of a Lorentzian function was  $10 \pm 2 \mu\text{eV}$ , which is comparable to  $\Gamma$  for a sulfide-based Li ionic conductor  $\text{Li}_7\text{P}_3\text{S}_{11}$  obtained using DNA [13].

From the fits at  $h = -1.0, -0.8, -0.6, -0.4, -0.2$  (rlu)

along the scan trajectory of [110] [Fig. 1(b)], the  $Q$  dependence of  $\Gamma$  was obtained at  $T = 410$  and  $600$  K [Fig. 3(a)], where  $Q$  is the magnitude of a wave vector from the origin. Because  $\Gamma$  increases quadratically with  $Q$  and saturates at a high  $Q$ , the obtained result suggests a translational jump diffusion of  $\text{Li}^+$  for  $T \geq 410$  K.

In the Chudley-Elliott (CE) model for the translational jump diffusion in Bravais lattices, the scattering function  $S(\mathbf{Q}, \omega)$  is given by [34]

$$S(\mathbf{Q}, \omega) = \frac{\exp(-2W)}{\pi} \frac{\Gamma(\mathbf{Q})}{\omega^2 + \Gamma(\mathbf{Q})^2}, \quad (1)$$

where  $\exp(-2W)$  is the Debye-Waller factor. Here,  $\Gamma(\mathbf{Q})$  is written as

$$\Gamma(\mathbf{Q}) = \frac{\hbar}{z\tau} \sum_j^z [1 - \exp(-i\mathbf{Q} \cdot \mathbf{l}_j)], \quad (2)$$

where  $\tau$  is the residence time,  $\mathbf{l}_j$  is the jump vector, and  $z$  is the number of sites. Because  $[1 - \exp(-i\mathbf{Q} \cdot \mathbf{l}_j)] = 0$  when  $\mathbf{Q} \perp \mathbf{l}_j$ ,  $\Gamma(\mathbf{Q})$  for the [110] direction reflects the  $\text{Li}^+$  jumps in the  $ab$  plane.

To infer the candidates of the  $\mathbf{l}_j$  in the  $ab$  plane, we conducted MD simulations using first-principles calculations of LLTO. The simulated trajectories of  $\text{Li}^+$  ions in the La-poor (La2) layer on the  $ab$  plane are shown in Fig. 4. For simplicity, we also assumed the absence of La ions at the La2 site in the simulations.  $\text{Li}^+$  ions move around the A sites, and the trajectories form a square shape with edges toward the  $a$  or  $b$  directions. The square trajectories are consistent with the distribution of  $\text{Li}^+$  ions determined from reverse Monte Carlo simulations based on the x-ray and neutron diffraction data [12, 13]. Note that some of the  $\text{Li}^+$  ions jump to the neighboring A site through the bottle neck structure, suggesting that the jump toward the vacant A site is the key pathway of  $\text{Li}^+$  diffusion.

Based on the information obtained from the MD calculations,  $\text{Li}^+$  ions are found to jump along the [100] and [010] directions in the  $ab$  plane. Therefore, Eq. (2) is rewritten as

$$\Gamma(\mathbf{Q}) = \frac{\hbar}{2\tau_{ab}} \left[ 2 - \cos\left(\frac{Q_x l_{ab}}{\sqrt{2}}\right) - \cos\left(\frac{Q_y l_{ab}}{\sqrt{2}}\right) \right]. \quad (3)$$

The observed  $\Gamma(\mathbf{Q})$  for the [110] direction are reproduced well by this model with  $\tau_{ab} = 0.11 \pm 0.01$  ns and  $l_{ab} = 3.9 \pm 0.4$  Å as indicated by the broken lines in Fig. 3(a). Note that the obtained  $l_{ab}$  is equivalent to the  $a$ -axis length of the cubic perovskite ( $a = 3.87$  Å) within the error bar. This is consistent with the result of the MD calculations, in which  $\text{Li}^+$  ions jump to the neighboring A site through the bottle neck.

For a small  $Q$  parallel to the jump vector, Eq. (2) is converted into the following:

$$\Gamma(Q) = \hbar \frac{l_j^2}{2\tau} Q^2 = \hbar D_{\text{Li}} Q^2, \quad (4)$$

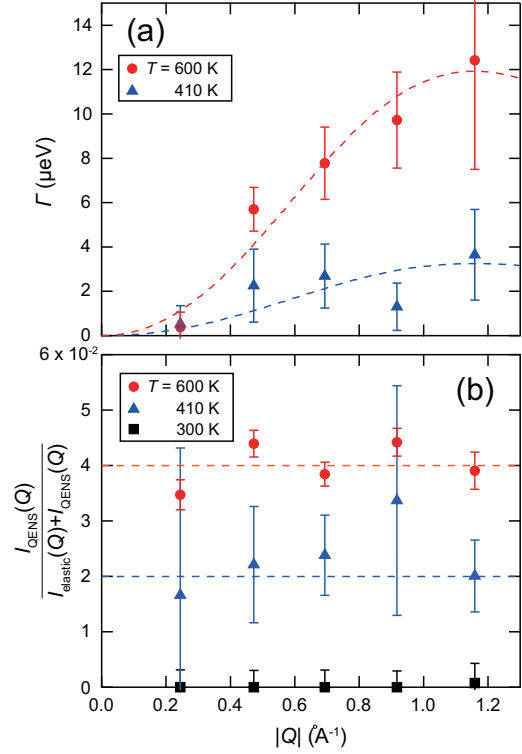


FIG. 3. (color online)  $Q$  dependences of (a) Lorentzian line width  $\Gamma$  and (b) QENS to total intensity ratio ( $V_{\text{QENS}}$ ) for the [110] scan trajectory, as described in the text.  $\Gamma$  is determined from the data averaged over  $\Delta h = \pm 0.1$  r.l.u. in  $(h h 0)$  at approximately  $h = -1.0, -0.8, -0.6, -0.4$ , and  $-0.2$  r.l.u. The magnitude of a wave vector from the origin  $Q$  is calculated at each point and  $\Gamma$  is plotted against  $Q$ .

where  $D_{\text{Li}}$  is a self-diffusion coefficient of  $\text{Li}^+$  ions. Thus,  $D_{\text{Li}}$  is estimated as  $6.8 \pm 0.5 \times 10^{-6}$   $\text{cm}^2/\text{s}$  at  $T = 600$  K directly from  $l_j^2/2\tau$ . Because the jump distance  $l$  is roughly independent of  $T$ ,  $\tau$  and  $D_{\text{Li}}$  are easily estimated at  $T = 410$  K (see Table II). Inaguma *et al.* reported the thermal activation energy ( $E_a$ ) of 0.15 eV at above 400 K from the bulk conductivity measurements [5]. The decrease in  $D_{\text{Li}}$  is in good agreement with the Arrhenius law with  $E_a$  of 0.15 eV. It is interesting to compare the present  $D_{\text{Li}}$  with that for  $\text{Li}_7\text{P}_3\text{S}_{11}$  estimated from the QENS data obtained with **DNA**: that is, for  $\text{Li}_7\text{P}_3\text{S}_{11}$ ,  $D_{\text{Li}} = 5.7 \times 10^{-6}$   $\text{cm}^2/\text{s}$  at  $T = 473$  K [18]. For LLTO,  $D_{\text{Li}}$  at  $T = 473$  K is estimated from  $D_{\text{Li}}$  at 600 K and  $E_a = 0.15$  eV as  $3.1 \pm 0.3 \times 10^{-6}$   $\text{cm}^2/\text{s}$ , which is close to that for  $\text{Li}_7\text{P}_3\text{S}_{11}$  (Table I). This means that a fast  $\text{Li}^+$  diffusion is achieved even in oxide-based  $\text{Li}^+$  ionic conductors, as well as in the sulfide-based conductors, from a microscopic perspective.

In addition to  $\Gamma(Q)$ , a fraction of the QENS component to the total intensity ( $V_{\text{QENS}}$ ), defined as

$$V_{\text{QENS}} = \frac{I_{\text{QENS}}(Q)}{I_{\text{elastic}}(Q) + I_{\text{QENS}}(Q)}, \quad (5)$$

provides useful information on the  $\text{Li}^+$  dynamics. Here,

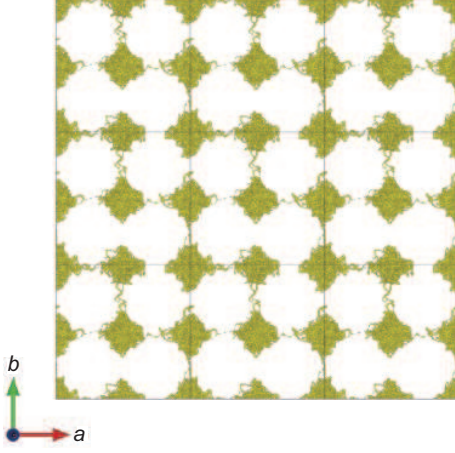


FIG. 4. (color online) Trajectories of  $\text{Li}^+$  ions in the  $ab$  plane of the La-poor layer simulated by MD using first-principles modeling for LLTO. The yellow traces show trajectories of  $\text{Li}^+$  ions.

$I_{\text{QENS}}(Q)$  and  $I_{\text{elastic}}(Q)$  are the integrated intensities of the QENS and elastic signal, respectively. For the translational diffusion, because only the Debye-Waller factor depends on  $Q$  in both  $I_{\text{QENS}}(Q)$  and  $I_{\text{elastic}}(Q)$ , such  $Q$  dependence is canceled out. Therefore,  $V_{\text{QENS}}$  is also independent of  $Q$  and is a good indicator for the number of mobile  $\text{Li}^+$  ions. In fact,  $V_{\text{QENS}}$  is roughly independent of  $Q$ , as shown in Fig. 3(b), which confirms the self-diffusive nature of the observed QENS signal at  $T = 600$  K and 410 K. The mobile  $\text{Li}^+$  ion fraction can be obtained by multiplying  $V_{\text{QENS}}$  by the ratio of the incoherent scattering cross section  $\sigma_{\text{inc}}$  of  $^7\text{Li}$  to the sum of  $\sigma_{\text{inc}}$  from all elements contained in LLTO, as summarized in Table II. The reduction in the fraction of mobile  $\text{Li}^+$  ions at lower  $T$  indicates the decrease in the number of mobile  $\text{Li}^+$  ions detectable in the time window of the current experimental setup.

Next, to determine the anisotropy of  $\text{Li}^+$  dynamics, the in-plane ([110])-QENS spectrum is compared with the out-of-plane ([001])-QENS spectrum at the same  $|Q| \sim 0.64 \text{ \AA}^{-1}$ . Figure 5 shows the spectra measured at  $T = 150$  and 600 K. At  $T = 600$  K, the [110]-QENS component is similar to the [001]-QENS component, indicating a nearly three-dimensional motion of  $\text{Li}^+$  ions. In fact, the two QENS spectra are well reproduced by the common  $\Gamma$  of  $7 \pm 2 \mu\text{eV}$ , whereas the QENS intensity of the in-plane motion is slightly larger than that of the out-of-plane motion.

Figure 6 shows the  $\Gamma(Q)$  curves at 600 K along the [110], [001], and [111] directions. For the [001] direction,  $\Gamma(Q)$  is described as

$$\frac{\hbar}{\tau_c} [1 - \cos(Q_z l_c)], \quad (6)$$

with  $l_c = 3.5 \text{ \AA}$  and  $\tau_c = 0.14 \text{ ns}$  (Table II). The jump length along the [001] direction ( $l_c$ ) is close to the  $a$ -axis length of the cubic cell, suggesting the jumps between

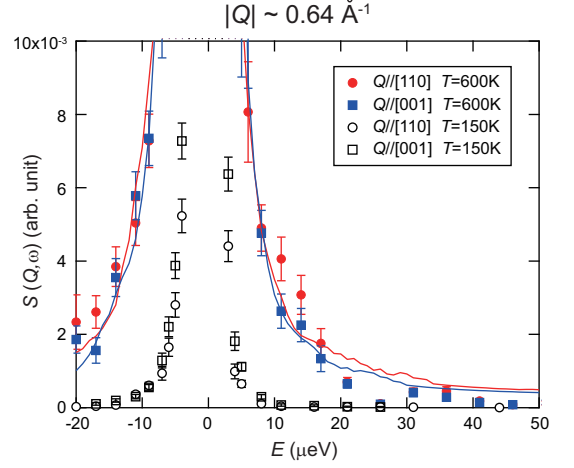


FIG. 5. (color online) In-plane ([110]) and out-of-plane ([001]) QENS spectra at  $|Q| \sim 0.64 \text{ \AA}^{-1}$  measured at  $T = 150$  and 600 K. To compare the intensity for different directions, neutron transmissions were corrected assuming a rectangular shape of the sample. The in-plane spectra were measured at  $(-0.55, -0.55, -0.11)$ , whereas the out-of-plane spectra were obtained at  $(0.09, 0.09, -0.80)$ . The solid lines represent the fits convolved with  $T = 150$  K data as instrumental resolution.

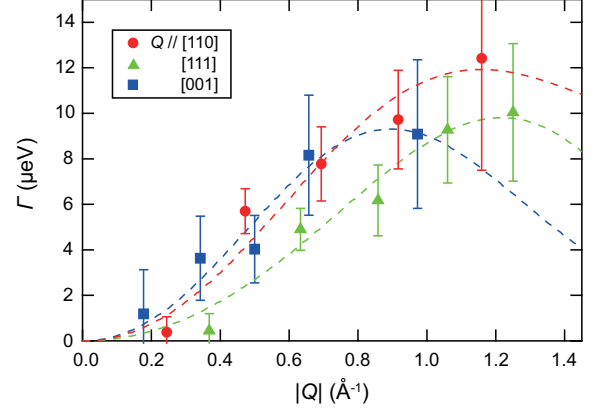


FIG. 6. (color online) (a)  $Q$  dependences of HWHM  $\Gamma$  of the Lorentzian component along three principal axes [110], [111], and [001] measured at  $T = 600$  K.

the  $A$ -sites of the neighboring Li/La planes [Fig. 1(a)]. Because  $\tau_{[001]}$  is slightly larger than  $\tau_{[110]}$ ,  $D_{\text{Li}[001]} < D_{\text{Li}[110]}$ . The  $\Gamma(Q)$  curve along the [111] direction is explained well by the coexistence of both jumps in the  $ab$  plane and along the  $c$  axis using the obtained QENS parameters for each direction.

#### IV. DISCUSSION

Returning to the Nernst-Einstein equation,  $D_{\text{Li}}$  is related to the ionic conductivity  $\sigma_{\text{Li}}$  as

$$\sigma = e^2 N D / k_B T, \quad (7)$$

TABLE II. Jump distance  $l$ , residence time  $\tau$ , diffusion coefficient  $D_{\text{Li}}$ , ratio of mobile  $\text{Li}^+$  ions, and the number of mobile  $\text{Li}^+$  ions  $N$  for LLTO ( $x = 0.13$ ).

Direction	$T$ (K)	$l$ (Å)	$\tau$ (ns)	$D_{\text{Li}}$ ( $10^{-6}$ cm <sup>2</sup> /s)	Ratio of mobile $\text{Li}^+$ ions(%)	$N$ ( $10^{27}$ m <sup>-3</sup> )
[110]	600	$3.9 \pm 0.4$	$0.11 \pm 0.01$	$6.8 \pm 0.5$	$50 \pm 1$	$3.35 \pm 0.07$
[110]	410	3.9 fix	$0.42 \pm 0.09$	$1.9 \pm 0.1$	$25 \pm 9$	$1.7 \pm 0.6$
[001]	600	$3.5 \pm 0.3$	$0.14 \pm 0.01$	$4.4 \pm 0.3$	$24 \pm 2$	$1.6 \pm 0.2$

where  $e$  is the elementary charge,  $N$  is the density of mobile  $\text{Li}^+$  ions, and  $k_{\text{B}}$  denotes the Boltzmann constant.  $N$  is estimated as  $3.35 \pm 0.07 \times 10^{27}$  m<sup>-3</sup> from the product of the mobile  $\text{Li}^+$  ion fraction and the number of  $\text{Li}^+$  ions ( $3x$ ) per cubic perovskite unit cell  $6.7 \times 10^{27}$  m<sup>-3</sup> (Table II). The microscopic  $\sigma_{\text{Li}}$  (hereafter denoted as  $\sigma_{\text{QENS}}$ ) at  $T = 600$  K is calculated as  $0.070 \pm 0.006$  S/cm and  $0.02 \pm 0.01$  S/cm for the in-plane and out-of-plane directions, respectively. The spatial average of the  $\sigma_{\text{QENS}}$   $0.055 \pm 0.005$  S/cm agrees with that of  $\sigma_{\text{Li}} \sim 0.1$  S/cm at  $T = 600$  K reported from bulk conductivity measurements for LLTO with slightly lower Li content ( $x = 0.11$ ) [5].

Table I summarizes  $\sigma_{\text{Li}}$ ,  $E_a$ , and  $D_{\text{Li}}$  for the sulfide-based  $\text{Li}^+$  ion conductors and LLTO. The  $\sigma_{\text{Li}}$  of LLTO is one or two orders of magnitude lower than that of the sulfur-based ones with relatively large  $E_a$ . The  $D_{\text{Li}}$  for LGPS and  $\text{Li}_7\text{P}_3\text{S}_{11}$  are the reported values obtained from pulsed field gradient nuclear magnetic resonance measurements (PFG-NMR), and they are considerably smaller than those of LLTO and  $\text{Li}_7\text{P}_3\text{S}_{11}$  despite their higher conductivity. Presumably, this is because QENS capture the dynamics of the smallest Li dynamic path, whereas PFG-NMR detects dynamics with longer length scale. Comparing the  $D_{\text{Li}}$  measured by QENS between LLTO and  $\text{Li}_7\text{P}_3\text{S}_{11}$ , the fact that  $D_{\text{Li}}$  for LLTO is comparable to that for  $\text{Li}_7\text{P}_3\text{S}_{11}$ , despite the difference in  $\sigma_{\text{Li}}$ , leads to the following question: what is the predominant factor for the difference in  $\sigma_{\text{Li}}$  between LLTO and  $\text{Li}_7\text{P}_3\text{S}_{11}$ ? The  $V_{\text{QENS}}$  for  $\text{Li}_7\text{P}_3\text{S}_{11}$  is 0.23 at  $T = 473$  K [35] and the fraction of mobile  $\text{Li}^+$  ions is 23%, which is similar to that for LLTO (Table II). Then,  $N$  is obtained as  $3.88 \times 10^{27}$  m<sup>-3</sup> by multiplying a Li ion density  $1.69 \times 10^{28}$  m<sup>-3</sup> for  $\text{Li}_7\text{P}_3\text{S}_{11}$ .  $N$  for LLTO at  $T = 473$  K is  $2.2 \times 10^{27}$  m<sup>-3</sup>, estimated from a linear interpolation between  $T = 410$  and  $600$  K, which is 1.7 times smaller than that of  $\text{Li}_7\text{P}_3\text{S}_{11}$ . Consequently,  $\sigma_{\text{QENS}}$  for  $\text{Li}_7\text{P}_3\text{S}_{11}$  is expected to be 3.2 times larger than that for LLTO according to the Nernst-Einstein equation. This is the most reasonable explanation for the difference in  $\sigma_{\text{Li}}$  between LLTO and  $\text{Li}_7\text{P}_3\text{S}_{11}$  at the microscopic scale.

Since the discovery of fast  $\text{Li}^+$  ionic conduction in sulfide-based  $\text{Li}^+$  ionic conductors [36], sulfide ions are considered to play a significant role in enhancing the mobility of  $\text{Li}^+$  ions through a large polarization. However, the fact that  $D_{\text{Li}}$  for LLTO is comparable to that

of  $\text{Li}_7\text{P}_3\text{S}_{11}$  indicates the possibility of better oxide-based  $\text{Li}^+$  ionic conductors by seeking materials with a larger Li density in the unit cell. Regarding the microscopic mechanism of fast  $\text{Li}^+$  diffusion, a coupling between the rotational motion of the  $\text{PS}_4^{3-}$  tetrahedra and  $\sigma_{\text{Li}}$  was indicated in the sulfide-based  $\text{Li}^+$  ionic conductors [37]. In LLTO, structural instabilities of the tilting modes of  $\text{TiO}_6$  tetrahedra are suggested from first-principles calculations [38]. Further studies on the dynamics of the host lattice of  $\text{Li}^+$  ionic conductors will be required to understand the mechanism of fast  $\text{Li}^+$  ionic conduction in solids.

## V. CONCLUSION

We studied the dynamics of  $\text{Li}^+$  ions in a solid-state electrolyte LLTO ( $x = 0.13$ ) using QENS and first-principles MD simulations. We observed clear QENS signals along the three principal axes [110], [111], and [001] at  $T = 600$  K by using the large  $^7\text{Li}$ -enriched single crystal. Directional information of the  $\text{Li}^+$  jump, such as the residence time and jump vector determined at the microscopic scale, reveals the dynamical conduction paths of  $\text{Li}^+$  ions: jumps of  $\text{Li}^+$  ions to the neighboring A site through the bottle neck structure, which are supported by the first-principles MD simulations. The self-diffusion coefficients of  $\text{Li}^+$  ions are found to be quasi-isotropic, suggesting the nearly three-dimensional diffusion of  $\text{Li}^+$  ions. Furthermore, the estimated self-diffusion coefficients of  $\text{Li}^+$  are comparable to those of the sulfide-based  $\text{Li}^+$  ion conductor  $\text{Li}_7\text{P}_3\text{S}_{11}$ , although the ionic conductivity of LLTO is 10 times smaller than that of  $\text{Li}_7\text{P}_3\text{S}_{11}$ . This microscopic information on  $\text{Li}^+$  diffusion can provide a way to increase  $\text{Li}^+$  ionic conductivity in oxide-based solid electrolytes.

## VI. ACKNOWLEDGEMENT

The neutron experiments were performed with the approval of J-PARC MLF (No. 2019A0306). We are grateful to K. Mori, M. Kofu, and J. Sugiyama for helpful discussions. We also thank M. Fujita and Y. Ikeda for their help with crystal alignment using a x-ray Laue diffractometer. The crystal structures in Fig. 1(a) are produced by VESTA software[39].

- 
- [1] J. M. Tarascon and M. Armand, *Nature* **414**, 171 (2001).
- [2] M. Armand and J.-M. Tarascon, *Nature (London)* **451**, 652 (2008).
- [3] N. Kamaya, K. Homma, Y. Yamakawa, M. Hirayama, R. Kanno, M. Yonemura, T. Kamiyama, Y. Kato, S. Hama, and K. Kawamoto, *Nat. Mater.* **10**, 682 (2011).
- [4] L. Latie, G. Villeneuve, D. Conte, and G. Le Flem, *J. Solid State Chem.* **51**, 293 (1984).
- [5] Y. Inaguma, C. Liquan, M. Itoh, T. Nakamura, T. Uchida, H. Ikuta, and M. Wakihara, *Solid State Commun.* **86**, 689 (1993).
- [6] Y. Inaguma, *J. Ceram. Soc. Jpn.* **114**, 1103 (2006).
- [7] J. L. Fourquet, H. Duroy, and M. P. Crosnier-Lopez, *J. Solid State Chem.* **127**, 283 (1996).
- [8] Y. Harada, T. Ishigaki, H. Kawai, and J. Kuwano, *Solid State Ionics* **108**, 407 (1998).
- [9] J. Ibarra, A. Várez, C. León, J. Santamaría, L. M. Torres-Martínez, and J. Sanz, *Solid State Ionics* **134**, 219 (2000).
- [10] D. Mazza, S. Ronchetti, O. Bohnké, H. Duroy, and J. L. Fourquet, .
- [11] Y. Inaguma, T. Katsumata, M. Itoh, Y. Morii, and T. Tsurui, *Solid State Ionics* **177**, 3037 (2006).
- [12] K. Ohara, Y. Kawakita, L. Pusztai, L. Temleitner, S. Kohara, N. Inoue, and S. Takeda, *J. Phys. Condens. Matter* **22**, 404203 (2010).
- [13] K. Mori, S. Tomihira, K. Iwase, and T. Fukunaga, *Solid State Ion.* **268**, 76 (2014).
- [14] A. Kuhn, V. Duppel, and V. B. Lotsch, *Energy Environ. Sci.* **6**, 3548 (2013).
- [15] A. Hayashi, S. Hama, H. Morimoto, M. Tatsumisago, and T. Minami, *J. Am. Ceram. Soc.* **84**, 477 (2001).
- [16] H. Stöffler, T. Zinkevich, M. Yavuz, A. Senyshyn, J. Kulisch, P. Hartmann, T. Adermann, S. Randau, F. H. Richter, J. Janek, *et al.*, *J. Phys. Chem. C* **122**, 15954 (2018).
- [17] Y. Onodera, K. Mori, T. Otomo, M. Sugiyama, and T. Fukunaga, *J. Phys. Soc. Jpn* **81**, 044802 (2012).
- [18] K. Mori, K. Enjuji, S. Murata, K. Shibata, Y. Kawakita, M. Yonemura, Y. Onodera, and T. Fukunaga, *Phys. Rev. Appl.* **4**, 054008 (2015).
- [19] See Supplemental Material for the details of the powder x-ray diffraction and the stability of FPMD simulations, which includes Refs. [11] and [20].
- [20] H.-T. Chung and D.-S. Cheong, *Solid State Ionics* **120**, 197 (1999).
- [21] Y. Fujiwara, K. Hoshikawa, and K. Kohama, *J. Cryst. Growth* **433**, 48 (2016).
- [22] I. A. Blech and B. L. Averbach, *Phys. Rev.* **137**, A1113 (1965).
- [23] J. P. Perdew, K. Burke, and M. Ernzerhof, *Phys. Rev. Lett.* **77**, 3865 (1996).
- [24] P. Hohenberg and W. Kohn, *Phys. Rev.* **136**, B864 (1964).
- [25] W. Kohn and L. J. Sham, *Phys. Rev.* **140**, A1133 (1965).
- [26] P. E. Blöchl, *Phys. Rev. B* **50**, 17953 (1994).
- [27] G. Kresse and J. Furthmüller, *Phys. Rev. B* **54**, 11169 (1996).
- [28] G. Kresse and D. Joubert, *Phys. Rev. B* **59**, 1758 (1999).
- [29] D. J. Evans and B. L. Holian, *J. Chem. Phys.* **83**, 4069 (1985).
- [30] K. Shibata, N. Takahashi, Y. Kawakita, M. Matsuura, T. Yamada, T. Tominaga, W. Kambara, M. Kobayashi, Y. Inamura, T. Nakatani, K. Nakajima, and M. Arai, *JPS Conf. Proc.* **8**, 036022 (2015).
- [31] Y. Inamura, T. Nakatani, J. Suzuki, and T. Otomo, *J. Phys. Soc. Jpn* **82**, SA031 (2011).
- [32] A. Várez, F. García-Alvarado, E. Morán, and M. A. Alario-Franco, *J. Solid State Chem.* **118**, 78 (1995).
- [33] J. Ibarra, A. Várez, C. León, J. Santamaría, L. M. Torres-Martínez, and J. Sanz, *Solid State Ionics* **134**, 219 (2000) .
- [34] R. Hempelmann, *Quasielastic Neutron Scattering and Solid State Diffusion* (Oxford : Clarendon Press, 2000).
- [35] K. Mori, personal communication.
- [36] R. Kanno, T. Hata, Y. Kawamoto, and M. Irie, *Solid State Ionics* **130**, 97 (2000).
- [37] J. G. Smith and D. J. Siegel, *Nat. Commun* **11**, 1 (2020).
- [38] H. Moriwake, X. Gao, A. Kuwabara, C. A. J. Fisher, T. Kimura, Y. H. Ikuhara, K. Kohama, T. Tojigamori, and Y. Ikuhara, *J. Power Sources* **276**, 203 (2015).
- [39] K. Momma and F. Izumi, *J. Appl. Cryst.* **44**, 1272 (2011).

**Supplemental material for**  
**Microscopic dynamics of lithium diffusion in single crystal of solid-state electrolyte**  
 **$\text{La}_{2/3-x}\text{Li}_x\text{TiO}_3$  ( $x = 0.13$ ) studied by quasi-elastic neutron scattering**

Masato Matsuura\*,<sup>1</sup> Yasuyuki Fujiwara,<sup>2</sup> Hiroki Moriwake,<sup>3</sup> Koji Ohara,<sup>4</sup> and Yukinobu Kawakita<sup>5</sup>

<sup>1</sup>*Neutron Science and Technology Center, Comprehensive Research Organization  
for Science and Society (CROSS), Tokai, Ibaraki 319-1106, Japan\**

<sup>2</sup>*Faculty of Engineering, Shinshu University, Nagano 380-8553, Japan*

<sup>3</sup>*Nanostructures Research Laboratory, Japan Fine Ceramics Center, Nagoya 456-8587, Japan*

<sup>4</sup>*Research and Utilization Division, Japan Synchrotron Radiation*

*Research Institute (SPring-8/JASRI), Sayo, Hyogo 679-5198, Japan*

<sup>5</sup>*Materials and Life Science Division, J-PARC Center, JAEA, Tokai, Ibaraki 319-1195, Japan*

(Dated: November 25, 2021)

### I. SUPPLEMENTARY MATERIAL

Figure S1 shows X-ray powder diffraction pattern of  $\text{La}_{2/3-x}\text{Li}_x\text{TiO}_3$  (LLTO) with  $x = 0.13$  used in this study. All reflections were indexed with Orthogonal cell [space group:  $Cmmm$ ,  $a(\sim 2a_p) \times b(\sim 2a_p) \times c(\sim 2a_p)$  [? ? ]], indicating no impurity phase in the sample.

To demonstrate the stability of first-principle molecular dynamics (FPMD) simulations in this study, here, we present certain plots of energy and temperature stability as a function of the simulation steps (40000). Drifts in the calculated temperature, ion-electron energy, and kinetic energy are shown in Fig. S2, Fig. S3, and Fig. S4, respectively. No significant drift was observed in the calculated temperature, ion-electron energy, and kinetic energy, confirming the stability of our FPMD simulations. Furthermore, the averaged temperature, ion-electron energy, and kinetic energy were controlled at  $1000 \pm 20$  K,  $330.8 \pm 0.5$  eV, and  $4.91 \pm 0.1$  eV, respectively.

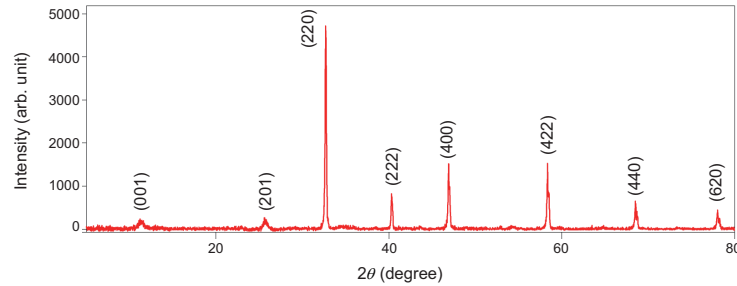


FIG. S1. (color online) Powder X-ray diffraction pattern of LLTO ( $x = 0.13$ ) used in this study.

---

\* m.matsuura@cross.or.jp

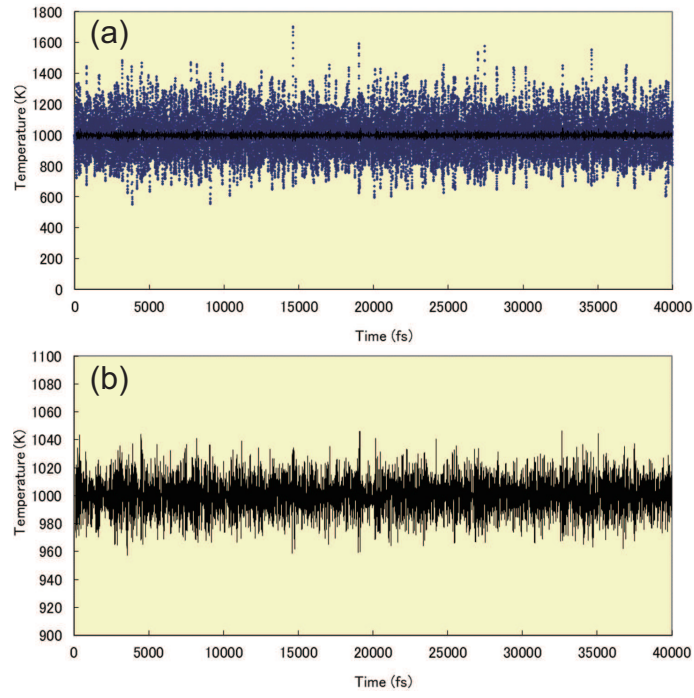


FIG. S2. (color online) (a) Temperature drift in the production run. The blue dots indicate calculated temperature, whereas the black line indicates average over 100 fs (step). (b) Enlarged plot of average temperature.

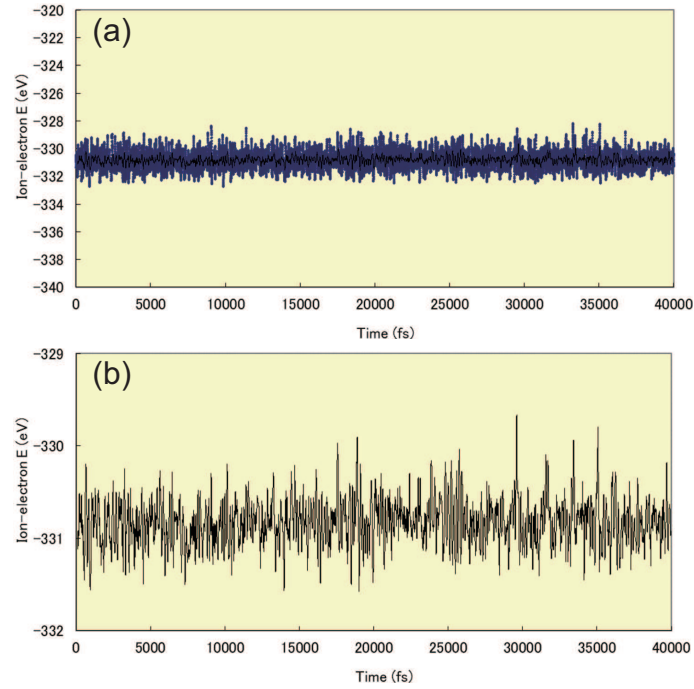


FIG. S3. (color online) (a) Ion-electron energy drift in the production run. The blue dots indicate calculated ion-electron energy, whereas the black line indicates average over 100 fs (step). (b) Enlarged plot of average ion-electron energy.

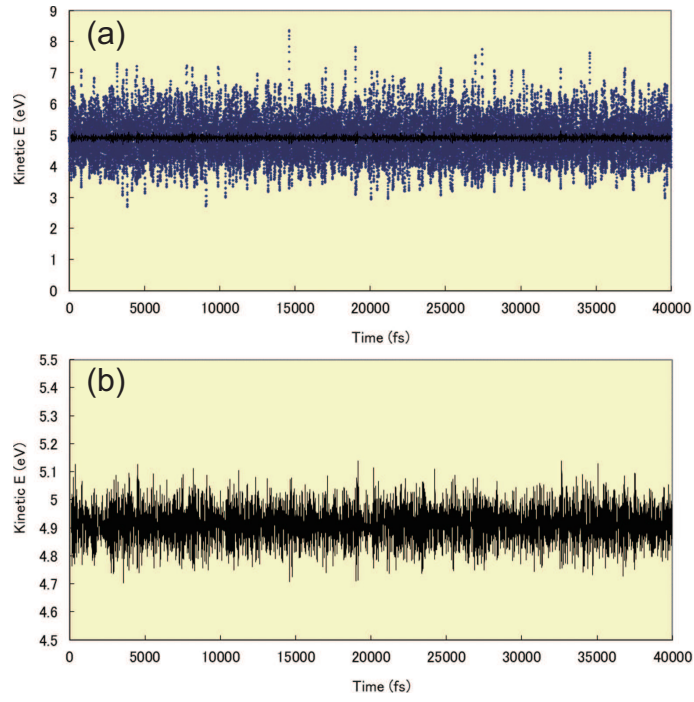


FIG. S4. (color online) (a) Kinetic energy drift in the production run. The blue dots indicate calculated ion-electron energy, whereas the black line indicates average over 100 fs (step). (b) Enlarged plot of average kinetic energy.